Structural connectivity-based segmentation of the human entorhinal cortex

Ingrid Framås Syversen [a],[*], Menno P. Witter [a], Asgeir Kobro-Flatmoen [a], Pål Erik Goa [b], Tobias Navarro Schröder [a], Christian F. Doeller [a],[c],[d]

[a] Kavli Institute for Systems Neuroscience, NTNU – Norwegian University of Science and Technology, MH, NTNU, Postbox 8905, Trondheim 7491, Norway
[b] Department of Physics, NTNU – Norwegian University of Science and Technology, Trondheim, Norway
[c] Max Planck Institute for Human Cognitive and Brain Sciences, Leipzig, Germany
[d] Institute of Psychology, Leipzig University, Leipzig, Germany

ABSTRACT

The medial (MEC) and lateral entorhinal cortex (LEC), widely studied in rodents, are well defined and characterized. In humans, however, the exact locations of their homologues remain uncertain. Previous functional magnetic resonance imaging (fMRI) studies have subdivided the human EC into posteromedial (pmEC) and anterolateral (alEC) parts, but uncertainty remains about the choice of imaging modality and seed regions, in particular in light of a substantial revision of the classical model of EC connectivity based on novel insights from rodent anatomy. Here, we used structural, not functional imaging, namely diffusion tensor imaging (DTI) and probabilistic tractography to segment the human EC based on differential connectivity to other brain regions known to project selectively to MEC or LEC. We defined MEC as more strongly connected with presubiculum and retrosplenial cortex (RSC), and LEC as more strongly connected with distal CA1 and proximal subiculum (dCA1pSub) and lateral orbitofrontal cortex (OFC). Although our DTI segmentation had a larger medial-lateral component than in the previous fMRI studies, our results show that the human MEC and LEC homologues have a border oriented both towards the posterior-anterior and medial-lateral axes, supporting the differentiation between pmEC and alEC.

1. Introduction

The entorhinal cortex (EC) is a part of the medial temporal lobe, and a central structure for memory formation and navigation (Eichenbaum et al., 2007; Moser and Moser, 2013; Suzuki and Eichenbaum, 2000). It is classically viewed as a hub for processing and relaying information from the neocortex to the hippocampus, and vice versa (Buzsáki, 1996; Lavenex and Amaral, 2000). The EC can be divided into two main subregions – 'medial' entorhinal cortex (MEC) and 'lateral' entorhinal cortex (LEC) – which differ in both functional properties and connectivity with other regions (Canto et al., 2008; Kerr et al., 2007; van Strien et al., 2009). Both the function and anatomy of the EC subregions have been widely studied in rodents and non-human primates. Based mainly on research in rodents, the MEC is associated with spatial processing in a global, allocentric frame of reference, given the prevalence of spatially modulated cells such as grid and head direction cells (Fyhn et al., 2004; Hafting et al., 2005; Høydal et al., 2019; Knierim et al., 2014). In contrast, the LEC contains cells that are sensitive to the presence of objects in a local frame of reference or processing of time (Deshmukh and Knierim, 2011; Knierim et al., 2014; Tsao et al., 2013, 2018). Although recent years have seen a stark in-

crease in functional magnetic resonance imaging (fMRI) studies of the human EC (Bellmund et al., 2019; Chen et al., 2019; Montchal et al., 2019; Maass et al., 2015; Navarro Schröder et al., 2015; Reagh and Yassa, 2014; Schultz et al., 2012), the exact locations of the human homologues of MEC and LEC remain uncertain.

While comprehensive entorhinal delineations based on cytoarchitectonic analyses exist (Insausti et al., 1995; Krimer et al., 1997), we cannot directly relate these to datasets obtained with MRI where the resolution does not cover the single neuron level. Moreover, also in the macaque monkey, the cytoarchitectonically defined subdivisions of EC have not yet yielded a clear distinction between what might be counterparts of MEC and LEC in the rodent, and it was suggested that connectional data might be a more fruitful approach (Witter and Amaral, 2021). This lack of clear defining criteria limits the interpretation of findings involving EC in humans assessed with the help of MR images. For example, an in-depth parcellation of the homologue regions of MEC and LEC in humans is highly important for our understanding of the role of the EC in spatial (Bellmund et al., 2016; Doeller et al., 2010; Howard et al., 2014) and temporal (Bellmund et al., 2019; Montchal et al., 2019) context representations for episodic memory and mnemonic behavior in general. Furthermore, results from rodent models of Alzheimer's disease indicate that the disease initially affects LEC (Khan et al., 2014), whereas

studies on humans show that the disease affects anterolateral parts of EC before more intermediate or posteromedial parts become affected (Berron et al., 2021; Kulason et al., 2019). Formulating criteria other than anatomical landmarks to define the counterpart of MEC and LEC in humans will therefore be directly relevant for design and interpretation of studies on their role in cognition and functional decline in rodent models in ways that allow for extrapolation to humans, and vice versa.

fMRI studies have indeed shown that certain properties of the rodent and non-human primate EC also apply to the human EC (Doeller et al., 2010; Reagh and Yassa, 2014; Schultz et al., 2012). Based on the subdivision of the rodent EC into MEC and LEC, studies have tried to localize their respective homologue regions in humans. Previous fMRI studies tested connectivity 'fingerprints' of EC subregions to other parts of the brain. Studies in rodents and non-human primates have demonstrated a largely similar organization of EC connectivity across species (Canto et al., 2008), thus predicting distinct fMRI connectivity fingerprints for the two subregions in humans as well. The resulting delineations of putative human homologue regions of the rodent MEC and LEC were labeled posteromedial EC (pmEC) and anterolateral EC (alEC), based on the outcome of two independent fMRI studies that tested local and global connectivity, respectively (Maass et al., 2015; Navarro Schröder et al., 2015). However, it remains unclear whether the results were affected by the nature of the imaging modality or the choice of seed brain regions used to identify the subregions.

In addition to the neuroimaging modality, the second reason for a re-evaluation has gained additional importance since the assumption about EC connectivity on which parts of the previous fMRI studies (Maass et al., 2015) were based on has been recently revised. For years, the existence of two parallel cortical connectivity streams through the EC has been the accepted model (Nilssen et al., 2019; Ranganath and Ritchey, 2012; Witter et al., 2017). This comprises one pathway into the hippocampus via the parahippocampal/postrhinal cortex (PHC/POR) and MEC (the "where" pathway), and a parallel pathway via the perirhinal cortex (PRC) and LEC (the "what" pathway). However, recent evidence substantially challenged this view. Doan and colleagues found that POR in rats, which corresponds to the PHC in humans, does also project to LEC. These authors further argue that existing data in monkeys substantiate this notion (Doan et al., 2019). This is in line with new findings in humans indicating that the hippocampal-entorhinal-neocortical connections are far more complex than a pure segregation into "where" and "what" pathways (Huang et al., 2021).

In order to identify the human homologues of MEC and LEC, we should take advantage of known unique connections to each subregion. For example, in rodents the presubiculum projects almost exclusively to MEC, whereas distal CA1 and proximal subiculum (dCA1pSub, i.e. the border region between CA1 and subiculum) project most strongly to LEC (Caballero-Bleda and Witter, 1993; Honda and Ishizuka, 2004; Witter and Amaral, 1991, 2021). Meanwhile, the retrosplenial cortex (RSC) and the lateral orbitofrontal cortex (OFC) are respectively selectively connected with MEC and LEC (Hoover and Vertes, 2007; Insausti and Amaral, 2008; Jones and Witter, 2007; Kondo and Witter, 2014; Saleem et al., 2008; Witter and Amaral, 2021; Wyss and Van Groen, 1992). To investigate the connectivity between these regions, there are several imaging modalities available. An alternative method to the widely used fMRI and functional connectivity is to study instead structural connectivity using diffusion tensor imaging (DTI), another type of MRI (Powell et al., 2004; Zeineh et al., 2012). Here, one exploits the diffusion of water molecules inside white matter tracts and uses this to map the paths of these fibers – so-called tractography (Mori et al., 1999; Mori and Zhang, 2006). Mapping DTI connectivity profiles from cortices that project selectively to either EC subregion could provide a novel line of evidence to identify MEC and LEC (Ezra et al., 2015; Máté et al., 2018; Saygin et al., 2011).

The objective of this study is therefore to identify the human homologues of the rodent MEC and LEC using DTI, incorporating the novel insights from rodent anatomy. To achieve this, we performed proba-

bilistic tractography on high-quality DTI data acquired by the Human Connectome Project (Fan et al., 2016). We identify the EC subregions by analyzing the connectivity profiles from regions of interest (ROIs) that project selectively to either of them and compare these to the results from previous fMRI studies.

2. Materials and methods

2.1. MRI data

Publicly available structural and diffusion MRI data from 35 healthy adults were obtained from the MGH-USC Human Connectome Project database (https://ida.loni.usc.edu, http://db.humanconnectome.org), in line with the MGH-USC HCP Data Agreement. All participants provided written informed consent, and the experiments were approved by the institutional review board of Partners Healthcare (Fan et al., 2016). The data were acquired on a Siemens 3T Connectom scanner with maximum gradient strength of 300 mT/m and slew rate 200 T/m/s (McNab et al., 2013; Setsompop et al., 2013). Structural T1-weighted images were acquired using a 3D magnetization-prepared rapid gradient-echo (MPRAGE) sequence at 1 mm isotropic resolution. Diffusion data were acquired using a spin-echo echo-planar imaging (EPI) sequence at 1.5 mm isotropic resolution, with b-values of 1000s/mm^2 (64 directions), 3000 s/mm^2 (64 directions), 5000 s/mm^2 (128 directions) and 10,000 s/mm^2 (256 directions). One non-diffusion-weighted ($b = 0$) image was collected every 14 image volumes.

2.2. Preprocessing

The MRI data were minimally preprocessed by the Human Connectome Project as described in Fan et al. (2014). In brief, this preprocessing pipeline included gradient nonlinearity correction, motion correction, Eddy current correction and b-vector correction.

2.2.1. Registration

Both structural and diffusion images were brain extracted using the brain mask from running the FreeSurfer (version 7.1.1, https://surfer.nmr.mgh.harvard.edu/) functions *recon-all* and *dt-recon* on the participant's structural and diffusion images, respectively (Fischl et al., 2002, 2004), before refining the result using the FMRIB Software Library's (FSL; version 5.0.9, http://fsl.fmrib.ox.ac.uk/fsl/) function BET (Jenkinson et al., 2012; Smith, 2002). For the diffusion images, brain extraction and registration were performed on the participant's average $b = 1000$ image. The individual brain-extracted structural and diffusion images were registered to each other, as well as to the MNI152–09b standard brain template (Fonov et al., 2009), using symmetric non-linear registration in the Advanced Neuroimaging Toolbox (ANTs; version 2.3.4, http://stnava.github.io/ANTs/) based on mutual information (Avants et al., 2011).

2.2.2. Regions of interest

Regions of interest (ROIs) including the EC, presubiculum, CA1 and subiculum were extracted from the automated cortical and subcortical parcellation obtained from running FreeSurfer's *recon-all* and *segmentHA_T1* functions on the MNI152-09b template (Fischl et al., 2002, 2004; Iglesias et al., 2015). The EC ROI was further refined by masking it by a probabilistic EC ROI, thresholded at 0.25 from the Jülich-Brain Cytoarchitectonic Atlas (Amunts et al., 2020). Since the resulting EC ROI extended too far posteriorly towards the parahippocampal cortex and laterally beyond the collateral sulcus, we also performed a manual adjustment. This manual adjustment comprised using the FSL function *fslmaths -ero* to erode the ROI once, before removing remaining voxels with an irregular appearance in posterior and lateral parts. We then created ROIs of distal CA1/proximal subiculum by splitting each of the two hippocampal structures in half along its proximodistal axis. Of all voxels encompassing CA1, the half located distally was included, and of all

the voxels encompassing subiculum, the half located proximally was included: these two halves thus make up what we here define and refer to as 'distal CA1/proximal subiculum' (dCA1pSub). To create RSC and OFC ROIs, respectively, the FreeSurfer parcellations named "isthmus cingulate" and "lateral orbitofrontal" were used as a starting point. The final RSC ROI was obtained by tailoring the isthmus cingulate and removing the excess superior areas, while the final OFC ROI was obtained by extracting the posterolateral quadrant of the lateral orbitofrontal area. All resulting ROIs are shown in Supplementary Fig. 1. The ROIs were registered to the participants' individual spaces by applying the calculated transformations from ANTs. To increase the anatomical precision of the ROIs, the registered ROIs were then masked by respective participant-specific FreeSurfer parcellations.

2.3. DTI analysis

All DTI analyses were performed in the participant's native diffusion space. Voxel-wise fiber orientation distribution functions (fODFs) were computed by running the FSL function *bedpostx* on the diffusion data, using the zeppelin deconvolution model, a Rician noise model, and burn-in period 3000 (Sotiropoulos et al., 2016). Probabilistic tractography between the EC and presubiculum, dCA1pSub, RSC and OFC ROIs was then performed by running FSL's *probtrackx2* on the fODFs (Behrens et al., 2007, 2003b). Tractography was performed both in ROI-by-ROI and voxel-by-ROI connectivity mode, with number of samples 250,000, minimal path length 5 mm, and a midline termination mask (Behrens et al., 2003a; Ezra et al., 2015; Johansen-Berg et al., 2004; Máté et al., 2018; Saygin et al., 2011). For tractography between EC and presubiculum, paths were excluded if they reached the dCA1pSub ROI, while for tractography between EC and dCA1pSub, paths were excluded if they reached the presubiculum ROI – and equivalently for tractography between EC and RSC/OFC. For both *bedpostx* and *probtrackx2*, parameters were run with default values unless otherwise specified. ROI-by-ROI connectivity mode provides probability maps of the connectivity paths between the ROIs, while voxel-by-ROI connectivity mode provides probability maps of the voxel-wise connectivity of the EC ROI with the other ROIs, respectively. All tractography results were registered to MNI space and further analyses were performed there to facilitate inter-participant comparisons.

2.4. MEC and LEC segmentation

The voxel-wise connectivity maps were normalized to [0,1] by dividing them by the maximum probability for each hemisphere separately, and then thresholded by 0.01 to reduce false positive connections (Behrens et al., 2003a; Saygin et al., 2011). This threshold was determined empirically by testing a range of thresholds and choosing the one that in most cases removed connections outside the gray matter, because due to remaining distortions in the DTI images some of the EC ROIs slightly extended into air voxels. Crucially, we then define the MEC as the region that is most strongly connected with the presubiculum and/or RSC, while the LEC is the region that is most strongly connected with dCA1pSub and/or OFC (Caballero-Bleda and Witter, 1993; Honda and Ishizuka, 2004; Hoover and Vertes, 2007; Insausti and Amaral, 2008; Jones and Witter, 2007; Kondo and Witter, 2014; Saleem et al., 2008; Witter and Amaral, 1991, 2021; Wyss and Van Groen, 1992). For each participant, a hard segmentation was performed on the normalized and thresholded voxel-wise connectivity maps using FSL's *find_the_biggest* (Behrens et al., 2003a; Johansen-Berg et al., 2004), meaning that the voxels that had a higher connection probability with the presubiculum/RSC than with dCA1pSub/OFC were classified as MEC, and vice versa for LEC.

2.5. Group analysis

Group probability maps of the connectivity paths between the ROIs, as well as group probability maps of voxel-wise connectivity, were created by summing and averaging all the individual maps. Inter-participant segmentation variability maps were created by adding together all the individual participants' MEC and LEC segmentations, respectively. Group MEC and LEC segmentation were performed similarly to the individual segmentation: The group voxel-wise connectivity maps were first smoothed with a Gaussian kernel of 1 mm and thresholded by 0.01, and then a hard segmentation was performed equivalently to the single-participant segmentation by comparing the connection probabilities of EC with presubiculum/RSC vs. dCA1pSub/OFC. Four different segmentations were performed with all the 2 × 2 combinations of seed regions, in addition to a combined segmentation approach where the connectivity maps for presubiculum + RSC and for dCA1pSub + OFC, respectively, were combined and averaged before segmentation.

2.6. Segmentation comparisons

To assess the different segmentation approaches and compare the resulting locations of MEC and LEC, we calculated the orientation of the MEC-LEC border along the posterior-anterior (PA) and medial-lateral (ML) axes, respectively. This was performed by first calculating the centers of gravity of the differently defined MECs and LECs, and the vector between these centers of gravity. Next, the angle between this vector and a pure PA or ML vector was determined. We defined the PA axis as the long axis of the hippocampus. The degree of PA- or ML-oriented border was then defined between 0 and 100% such that an angle of 0° to the PA or ML vector means that the border is 100% oriented along the PA or ML vector, respectively. Correspondingly, an angle of 90° would mean that the border is 0% oriented along the respective axis, i.e. it is orthogonal to that axis. In addition, the different segmentations were compared with respect to the sizes of the resulting MECs and LECs, and the size ratios between these were calculated. All these segmentation comparisons were also carried out on the two fMRI-based segmentations of pmEC and alEC available for download from earlier studies (Maass et al., 2015; Navarro Schröder et al., 2015).

3. Results

To qualitatively visualize the connectivity paths between the EC and the regions hypothesized to be connected with its subregions, we ran probabilistic tractography between the regions. By seeding paths from all voxels in the EC, presubiculum, dCA1pSub, RSC and OFC ROIs, maps of the connectivity paths between the EC and the other ROIs were created. The resulting group averaged paths are shown in Fig. 1. In all figures, blue color schemes are used for MEC-related regions, i.e. presubiculum and RSC, while red color schemes are used for LEC-related regions, i.e. dCA1pSub and OFC. The maps show that all the regions exhibit clear connectivity with the EC. Connections with dCA1pSub extend further anteriorly in the EC than the connections with the presubiculum, and the connections with presubiculum and RSC seem to take a similar route to the EC. The paths between OFC and EC, however, stand out from the others as they take a more lateral route, but the inferior part seems to pass close to dCA1pSub. Note that the colormap intensity in these maps does not represent the actual number of white matter tracts, but instead scales with the probability that the true path between the ROIs lies in that point. Corresponding connectivity paths for one example participant are shown in Supplementary Fig. 2.

Because we wanted to segment the EC into the MEC and LEC homologues based on the connectivity with other regions, a voxel-by-voxel measure of connectivity probability was needed. We therefore also ran the tractography only seeding from the EC ROIs. Then, for each voxel in the ROI, we counted how many of the seeded paths reached the other
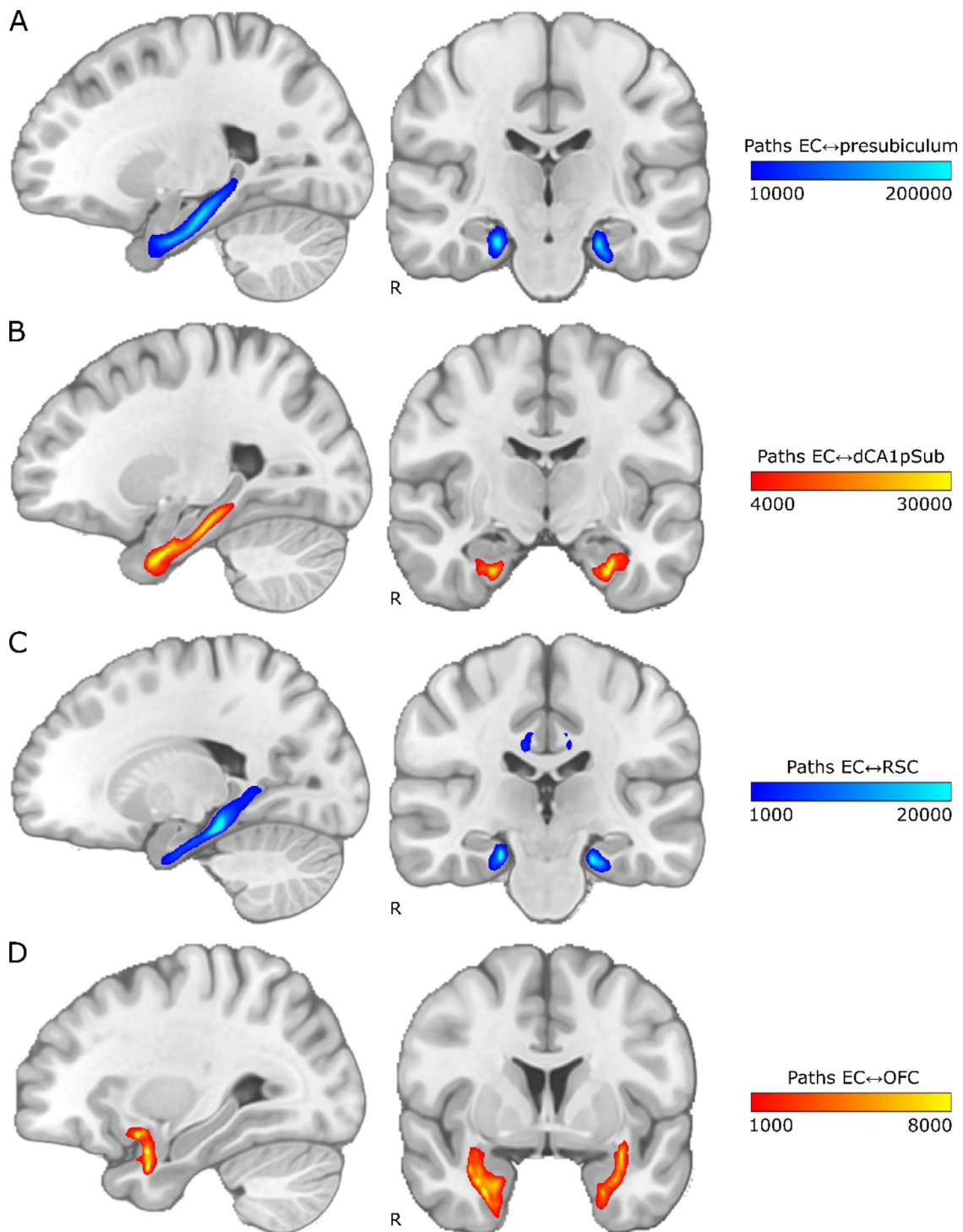
Fig. 1. Group average connectivity paths between EC and presubiculum, dCA1pSub, RSC and OFC. Connectivity patterns are shown on sagittal (left) and coronal (right) slices in MNI space, with "R" denoting the right side of the brain. The colormap intensity represents the number of probabilistic paths running through that voxel. A: Paths between EC and presubiculum, B: Paths between EC and dCA1pSub, C: Paths between EC and RSC, D: Paths between EC and OFC. (For interpretation of the references to color in this figure, the reader is referred to the web version of this article.)

ROIs. These connectivity counts were normalized to a probability, providing connectivity maps for the EC with the other four ROIs. The resulting smoothed and thresholded group averaged connectivity maps are shown in Fig. 2. The sagittal slices show that the connectivity with presubiculum and RSC appears to be strongest in the posterior part of the EC, whereas the connectivity with dCA1pSub and OFC is strongest anteriorly in the EC. Further, the presubiculum connectivity does not show a clear medial-lateral gradient, but the connections with dCA1pSub, RSC and OFC are stronger laterally in the EC in the selected coronal slices. Corresponding connectivity maps for one example participant are shown in Supplementary Fig. 3.

For segmentation into the MEC and LEC homologues, the main hypothesis was that these regions could be identified based on connectivity with presubiculum vs. dCA1pSub, respectively. The actual seg-
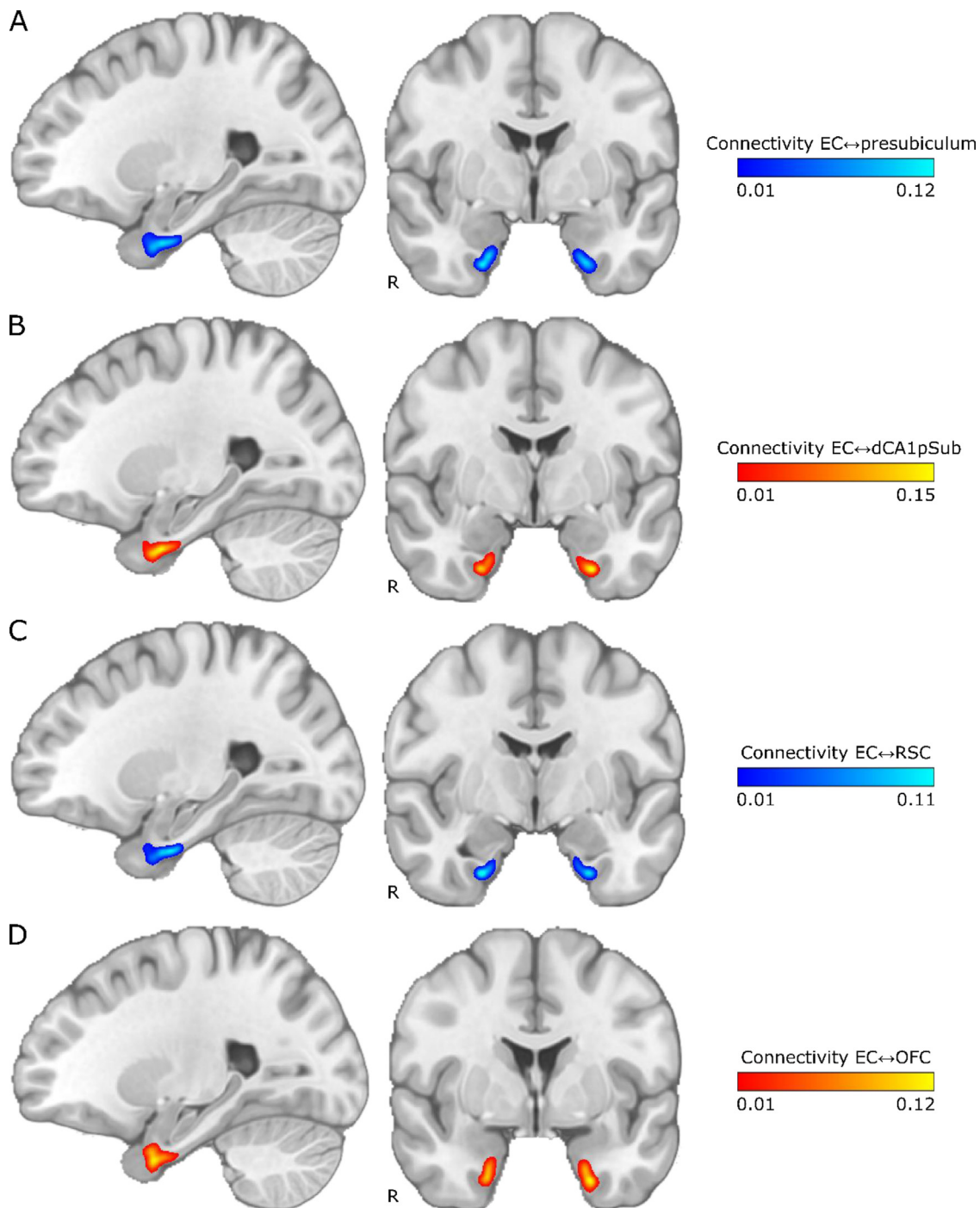
Fig. 2. Group average maps of EC connectivity with presubiculum, dCA1pSub, RSC and OFC. The maps are shown on sagittal (left) and coronal (right) slices in MNI space, with "R" denoting the right side of the brain. The colormap intensity represents the fraction of paths seeded from that EC voxel that reached the other ROI. A: EC connectivity with presubiculum, B: EC connectivity with dCA1pSub, C: EC connectivity with RSC, D: EC connectivity with OFC. (For interpretation of the references to color in this figure, the reader is referred to the web version of this article.)

mentation was performed on a voxel-by-voxel level in the EC determining with which of the other two regions the connection probability was highest, using the connectivity maps described in the previous paragraph. For comparison, the MEC-LEC segmentation was also performed based on connectivity with RSC vs. OFC, respectively. This was first performed individually for all participants, and inter-participant segmentation variability maps for the presubiculum vs. dCA1pSub and RSC vs. OFC segmentation approaches are shown in Fig. 3. For most participants, MEC is clearly located more posteriorly and LEC is located more

anteriorly for both segmentation approaches, and in addition they are located more medially and laterally with respect to each other for the presubiculum vs. dCA1pSub approach. The RSC vs. OFC approach also shows this medial-lateral trend of MEC and LEC across participants, although not as clear as for presubiculum vs. dCA1pSub. Corresponding MEC and LEC segmentations for one example participant are shown in Supplementary Fig. 4.

The same connectivity-based MEC-LEC segmentation was performed on a group level using the group averaged connectivity maps from Fig. 2.
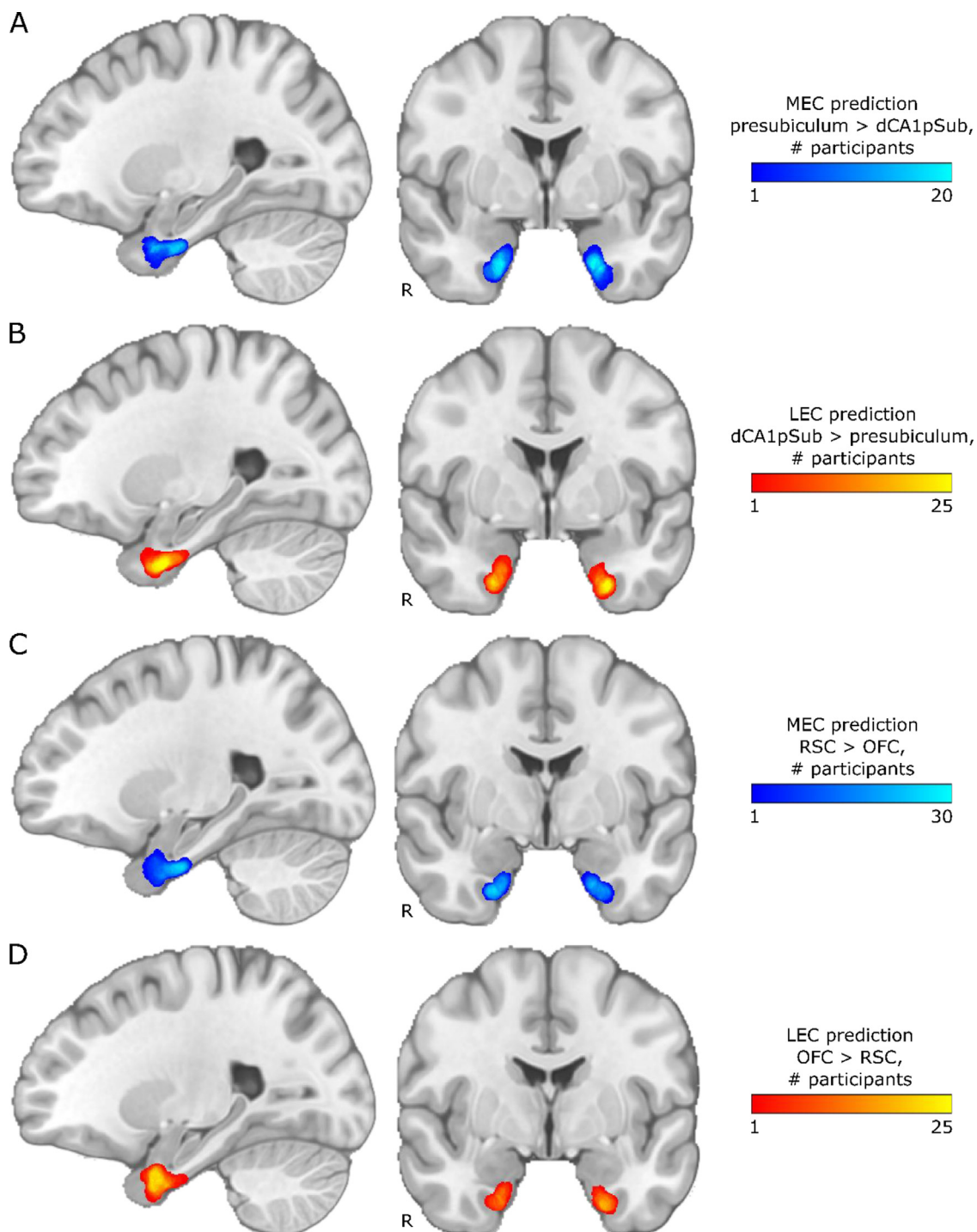
Fig. 3. Inter-participant segmentation variability maps for different segmentation approaches. Results are shown on sagittal (left) and coronal (right) slices in MNI space, with "R" denoting the right side of the brain. The colormap intensity represents the number of participants for which that voxel was classified as MEC or LEC, respectively. A: MEC prediction based on higher connectivity with presubiculum than with dCA1pSub, B: LEC prediction based higher connectivity with dCA1pSub than with presubiculum, C: MEC prediction based on higher connectivity with RSC than with OFC, D: LEC prediction based on higher connectivity with OFC than with RSC. (For interpretation of the references to color in this figure, the reader is referred to the web version of this article.)

As described above, the group segmentation was also performed using two different approaches – presubiculum vs. dCA1pSub, and RSC vs. OFC – and the resulting segmentations are shown in Fig. 4. We see that for the MEC and LEC predictions from presubiculum vs. dCA1pSub, there is a clear medial-lateral (ML) and posterior-anterior (PA)-oriented border between the subregions. For RSC vs. OFC, however, the PA-oriented border is most prominent, but it is also slightly ML-oriented,

most visible in the left EC. Because the results from the two approaches were slightly different, we also tried to interchange the ROI combinations, and MEC and LEC segmentations from using presubiculum vs. OFC and RSC vs. dCA1pSub can be seen in Supplementary Fig. 5. Furthermore, to include all the information from the 2 × 2 combinations of seed regions into one final segmentation, we performed another approach where we averaged the connectivity maps for presubiculum and
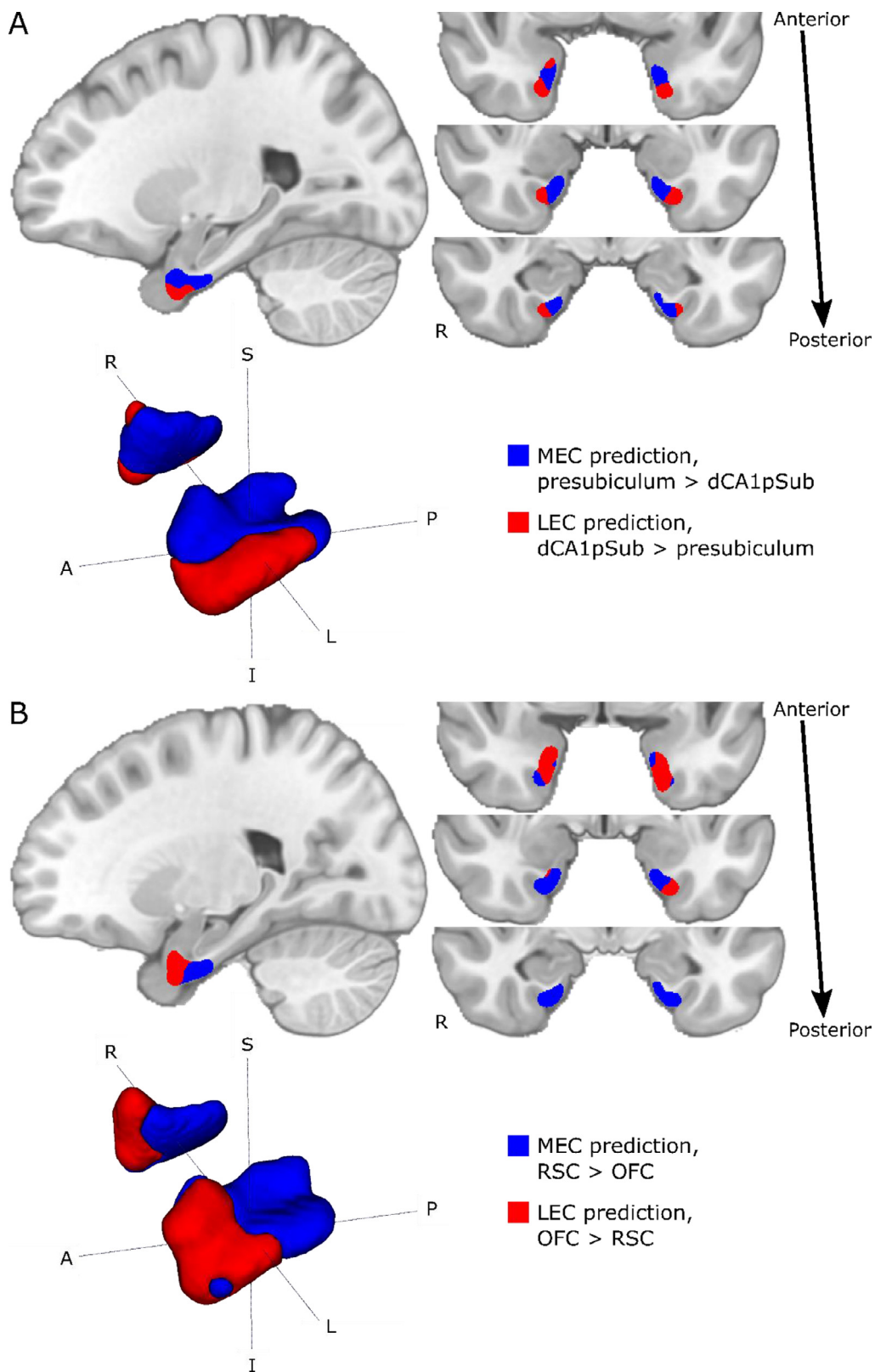
Fig. 4. Group segmentations of MEC and LEC from different approaches. Results are shown on sagittal (top left) and coronal (top right) slices and 3D-rendered (bottom left) in MNI space. The MEC and LEC predictions are shown in blue and red, respectively. A: MEC and LEC prediction based on connectivity with presubiculum vs. dCA1pSub, B: MEC and LEC prediction based on connectivity with RSC vs. OFC. S = superior, I = inferior, A = anterior, P = posterior, R = right, L = left. (For interpretation of the references to color in this figure legend, the reader is referred to the web version of this article.).

Table 1

Degree of posterior-anterior (PA) or medial-lateral (ML)-orientation of the border between MEC and LEC for different segmentation approaches. The degree of PA- or ML-orientation is given as a percentage between 0 and 100%, dependent on the angle between the MEC-LEC center of gravity vector and the pure PA or ML vector, respectively. All numbers are given as the mean of both hemispheres ± mean absolute deviation.

Segmentation approach		Posterior-anterior (PA) axis		Medial-lateral (ML) axis	
		Angle (°)	% PA	Angle (°)	% ML
DTI	Presubiculum/dCA1pSub	45.1 ± 3.0	49.9 ± 3.3	29.8 ± 1.9	66.9 ± 2.1
	RSC/OFC	39.7 ± 15.3	55.9 ± 17.0	84.5 ± 11.1	6.1 ± 12.3
	Presubiculum/OFC	41.3 ± 17.3	54.1 ± 19.3	81.2 ± 10.3	9.8 ± 11.5
	RSC/dCA1pSub	33.9 ± 1.2	62.3 ± 1.3	64.9 ± 18.8	27.9 ± 20.9
	Presubiculum+RSC/dCA1pSub+OFC	37.5 ± 10.6	58.3 ± 11.8	73.1 ± 17.4	18.7 ± 19.3
fMRI	Navarro Schröder et al.	6.8 ± 1.8	92.4 ± 2.0	85.5 ± 0.7	5.0 ± 0.8
	Maass et al.	6.6 ± 0.5	92.7 ± 0.6	87.9 ± 0.9	2.4 ± 1.0

Table 2

Resulting sizes of MEC and LEC for different segmentation approaches, and the size ratio between MEC and LEC. The numbers of voxels are given for the ROIs in MNI space with 0.5 mm isotropic resolution.

Segmentation approach		Size (# voxels)		MEC/LEC size ratio
		MEC	LEC	
DTI	Presubiculum/dCA1pSub	12,759	7763	1.64
	RSC/OFC	12,971	8727	1.49
	Presubiculum/OFC	13,614	6979	1.95
	RSC/dCA1pSub	11,045	10,282	1.07
	Presubiculum+RSC/dCA1pSub+OFC	13,571	7379	1.84
fMRI	Navarro Schröder et al.	12,802	16,028	0.80
	Maass et al.	3776	11,008	0.34

RSC, and the maps for dCA1pSub and OFC (Fig. 5A and B). Fig. 5C shows the resulting MEC and LEC homologues from this combined segmentation approach. With this approach, as with separate combinations of seed regions, we find both a PA- and ML-oriented (although most visible in the left hemisphere) border between MEC and LEC. These final MEC and LEC masks are also available in the Supplementary files.

In a next step, since the borders of the segmentations from different approaches showed slightly different orientations along the posterior-anterior (PA) and medial-lateral (ML) axes, we wanted to quantify this directional difference by calculating the "degree" of PA- and ML-orientation of the borders. This was defined as a percentage from 0 to 100%, dependent on the angle between the MEC-LEC center of gravity vector and a pure PA or ML vector. Table 1 shows the resulting degrees of PA- vs. ML- oriented borders for the different segmentation approaches including the fMRI segmentations from previous studies (Maass et al., 2015; Navarro Schröder et al., 2015). The center of gravity vectors are also plotted in a common reference frame in Supplementary Fig. 6. All DTI segmentation approaches have a border with a PA-orientation of around 50–60%, and a varying degree of ML-orientation from 6% for RSC vs. OFC up to 67% for presubiculum vs. dCA1pSub. The borders between the segmentations from fMRI have a high PA-orientation of around 92%, and a lower degree of ML-orientation than all of the DTI approaches. Interestingly, when comparing the different combinations of DTI approaches, using dCA1pSub as the defining region for LEC yields a higher degree of ML-orientation than using OFC. Similarly, using RSC as the defining region for MEC yields a slightly higher degree of PA-orientation of the border than using presubiculum, but this is less prominent.

Finally, we wanted to compare the resulting sizes of the MEC and LEC homologues from all the different segmentation approaches, and these are shown in Table 2. For all DTI approaches, the MEC is larger than LEC, while fMRI on the other hand yields a larger LEC than MEC. The subregions are most equally sized when using the RSC vs. dCA1pSub approach.

4. Discussion

In this study, we used DTI and probabilistic tractography in 35 healthy adults to segment the human EC into homologues of what in other mammals have been functionally, connectionally, and cytoarchitectonically defined as MEC and LEC. We based the segmentation on EC connectivity with four brain regions known to selectively project to either of the EC subregions in multiple species. Different combinations of these four regions all showed both a posterior-anterior (PA) and a medial-lateral (ML)-oriented border between the human homologues of MEC and LEC. This orientation of the thus defined border is similar to that defined in previous fMRI studies resulting in the definition of the two subregions as pmEC and alEC (Maass et al., 2015; Navarro Schröder et al., 2015). Note however that our DTI results show a larger degree of ML-orientation, and a correspondingly lower degree of PA-orientation of the border between the subregions compared to the previous fMRI results.

The results from our study substantiate the pmEC and alEC subdivision of the human EC suggested in previous fMRI studies (Maass et al., 2015; Navarro Schröder et al., 2015). Although some earlier fMRI studies on mnemonic processing in the EC found a dissociation primarily along the medial-lateral axis (Reagh and Yassa, 2014; Schultz et al., 2012), it is important to realize that even the orientation of the cytoarchitectonically defined border between MEC and LEC in rodents does not align along a pure medial-to-lateral axis. Rather, the MEC in rodents is located in the posterior-medial EC, and the LEC is located in the anterior-lateral EC (van Strien et al., 2009). Also, in macaque monkeys, tracing studies show differential connectivity in caudal vs. rostral portions (Witter and Amaral, 2021). A pure medial-lateral subdivision of human EC is thus not to be expected. Nevertheless, the somewhat different orientations of the border between the human homologues of MEC vs. LEC subdivisions found using DTI vs. fMRI studies raises the question of which of the two imaging modalities should be preferred to define the position and orientation of this border.
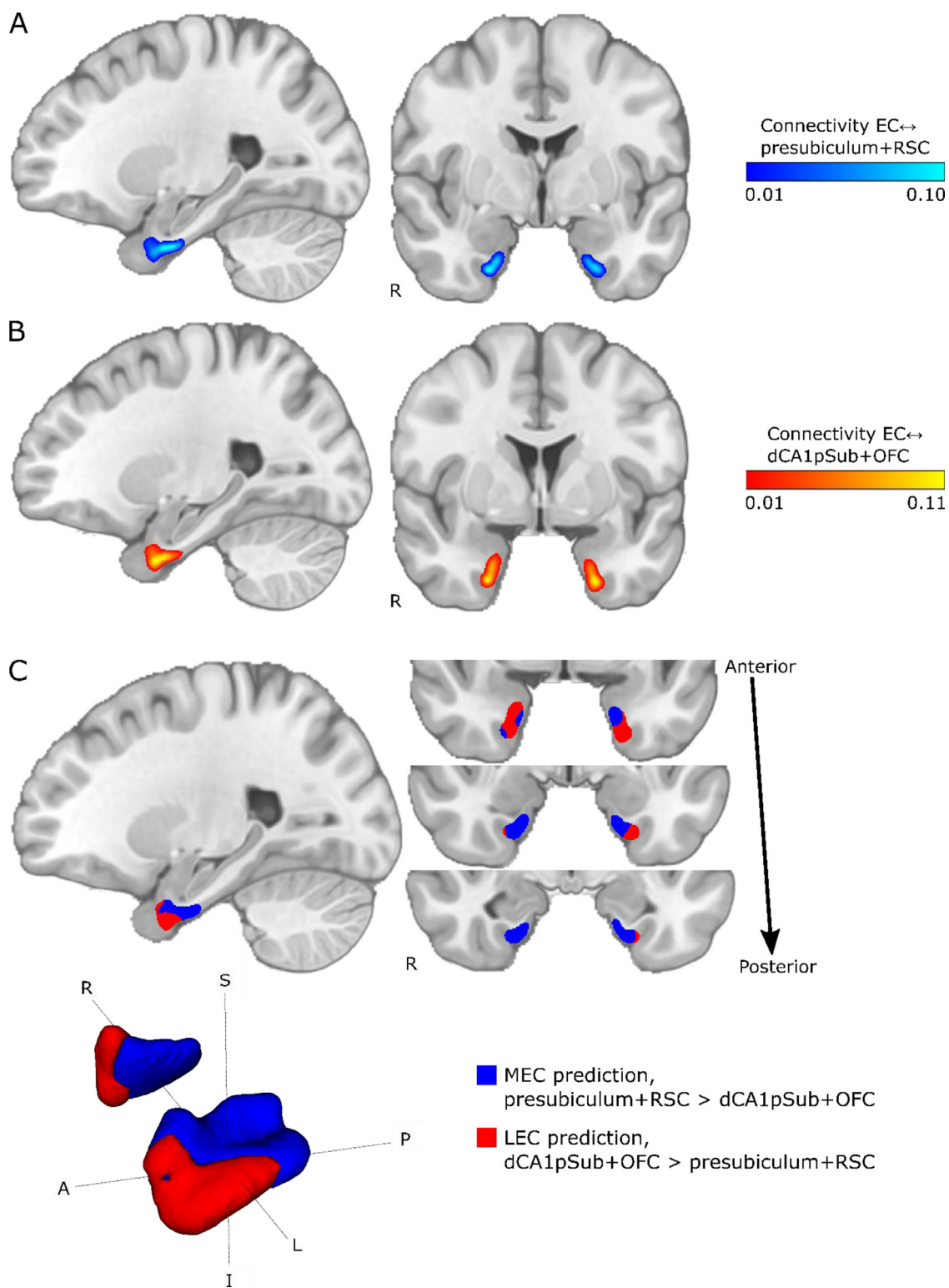
Fig. 5. Group connectivity maps and segmentation using a combined approach with presubiculum + RSC vs. dCA1pSub + OFC. A: EC connectivity with presubiculum + RSC combined. B: EC connectivity with dCA1pSub + OFC combined. C: MEC and LEC prediction based on connectivity with presubiculum + RSC vs. dCA1pSub + OFC combined. S = superior, I = inferior, A = anterior, P = posterior, R = right, L = left. (For interpretation of the references to color in this figure, the reader is referred to the web version of this article.)

There are several possible explanations as to why our DTI study showed slightly different segmentation results than the fMRI studies. First, DTI and fMRI are two different imaging modalities with inherently different mechanisms of connectivity. While DTI exploits the diffusion of water molecules in order to trace the structural paths of connectivity between brain regions (Mori et al., 1999; Mori and Zhang, 2006; Powell et al., 2004; Zeineh et al., 2012), fMRI identifies functional connectivity by correlating blood-oxygen-level-dependent (BOLD) signals across time (Van Dijk et al., 2010). Although structural and functional connectivity in theory should be closely linked, they are in reality quantitatively difficult to compare because of the complexity of the connectivity mechanisms of the brain (Huang and Ding, 2016; Messé et al., 2015). Another reason for the different results between the current and the previous studies could be the use of different seed regions to identify the MEC and LEC homologues. While we used presubiculum and RSC to define MEC, and dCA1pSub and OFC to define LEC (Caballero-Bleda and Witter, 1993; Honda and Ishizuka, 2004; Hoover and Vertes, 2007; Jones and Witter, 2007; Kondo and Witter, 2014; Saleem et al., 2008; Witter and Amaral, 1991, 2021; Wyss and Van Groen, 1992), one of the fMRI studies investigated differential connectivity of PHC vs. PRC and distal vs. proximal subiculum (Maass et al., 2015), whereas the other used regions in a posterior-medial vs. an anterior-temporal cortical system (Navarro Schröder et al., 2015). The new insights from rodent anatomy indicate that while PHC area TH is connected with the MEC, PHC area TF is connected with the LEC (Witter and Amaral, 2021). As area TF is located more laterally than TH, this might in part explain why the previous fMRI study where they used connectivity with the whole PHC to define the pmEC (Maass et al., 2015) showed a lower medial-lateral component of their pmEC-alEC segmentation than our results. In order to determine to which extent each of these reasons contributed to the different subdivision results across studies, both imaging modalities with identical seed regions should be investigated and compared more rigorously in one single, larger cohort of participants.

Interestingly, using different seed regions to identify MEC and LEC resulted in varying degrees of PA- and ML-orientation of the border between them. It is unclear whether this is inherently linked to the DTI method, or due to an actual connectivity difference between the regions. Using presubiculum and dCA1pSub as the seed regions, which are situated medially and laterally with respect to each other, respectively, resulted in a border with higher degree of ML- than PA-orientation. On the other hand, using RSC and OFC, which are situated posteriorly and anteriorly in the brain, respectively, resulted in a border with higher degree of PA- than ML-orientation. Although it is not unnatural to assume that the brain is organized such that connected regions are situated more closely to each other, this could also be an effect of using probabilistic tractography, where the apparent connectivity probability depends on e.g. the length of the path and the size of the ROIs (Behrens et al., 2007). In other species, including rodents and monkeys, the presubiculum and RSC show inputs to the EC with a similar spatial distribution (Witter and Amaral, 2021), aligning with our maps of connectivity paths with these two seed regions. However, comparing the different MEC and LEC segmentations from the different seed region combinations shows that while interchanging presubiculum and RSC yields only slightly different orientation of the border along the PA and ML axes, the difference when interchanging dCA1pSub and OFC is more substantial. In other species, dCA1pSub are known to project to both rostral and dorsolateral parts of EC, whereas posterolateral OFC mainly projects dorsolaterally in the EC (Insausti and Amaral, 2008; Kondo and Witter, 2014; Saleem et al., 2008; Witter and Amaral, 1991, 2021). Whether these regions in humans project to different parts of the homologue of LEC, or whether our results are affected by using DTI and probabilistic tractography, should be further investigated by also comparing EC functional connectivity to these areas using fMRI. Note also that the topography of projections from dCA1pSub along the medial-lateral axis of the EC depends on where the seed is placed along the posterior-anterior axis of the dCA1pSub (Witter and Amaral, 2021), which emphasizes the im-

portance of carefully defined seed ROIs. In addition, even more areas hypothesized to be preferentially connected to MEC or LEC should be evaluated in the future.

In order to determine and compare the connectivities between the EC and the other ROIs, we normalized the connectivity maps by dividing them by the maximum probability of each map. This could introduce a bias in the results. By doing this, we intrinsically assume that the maximum connectivity strength to each of the other ROIs are equal, and the segmentation process does not take into account that the MEC connections might be stronger than the LEC connections, or vice versa. However, little is known about the strength of connectivities at this level of detail, particularly since it is not straightforward to examine or even define connectivity strength. Connectivity strength surely depends on axonal density, but other factors like synaptic density and efficacy are other important variables. Nevertheless, even if we were to know that some of the connections are stronger than the others, probabilistic tractography provides a relative instead of an absolute measure of connectivity and is also dependent on path lengths, ROI sizes and the number of possible path directions in a voxel. Normalizing the connectivity maps based on different connectivity strengths would therefore be a highly complex task. Therefore, we did not impose any further assumptions about connectivity strengths in our analyses.

Performing tractography between the EC and the four other ROIs showed clear connectivity paths between the areas. The purpose of this analysis was to verify that the hypothesized seed regions were indeed structurally connected with the EC. However, characterization of the trajectories of these paths, including their differential distribution within the white matter of the angular bundle, was outside the scope of our study. Although qualitatively similar probabilistic paths between the EC and the subicular cortices have been shown in previous *ex vivo* DTI data (Augustinack et al., 2010), the large difference in spatial resolution between the studies makes a direct comparison difficult. This is nevertheless an interesting topic that could be addressed in future studies.

Our study has some limitations. To define our ROIs, we chose to use regions from automatic cortical segmentation protocols. This could have influenced the anatomical precision of our analysis. Manual segmentation would be labor-intensive and requires high skills in neuroanatomy, possibly limiting the number of participants that could be included in the study. However, we manually adjusted some of the automatically segmented ROIs, and also intersected the registered ROIs from MNI space with the participants' individual automatic segmentations in order to increase the anatomical accuracy. Another limitation is that there are inherent challenges to the EPI sequence used for diffusion imaging. This results in a generally low signal-to-noise ratio in the EC and the whole medial temporal lobe. In addition, these regions appear geometrically distorted in the EPI images, and although this has been corrected for, it is not possible to recover all of the lost signal. Imperfect correction can also affect the accuracy of the ROIs. Because of the probabilistic nature of the tractography technique it is unlikely that noise will introduce false significant connections, but it can leave some connections undetected. At last, a relatively low number of participants were included in our study, which might have influenced the statistical power of the results.

5. Conclusions

Our DTI results support the definition of pmEC and alEC as human homologues of MEC and LEC as they are currently connectionally defined in rodents and to a somewhat lesser extent in monkeys. Inspired by novel insights coming from rodent anatomy, we present a segmentation based on a combination of differential presubiculum/RSC and dCA1pSub/lateral OFC structural connectivity which indicates a border between the two subdivisions of EC with an orientation that is angled both towards the posterior-anterior axis, as well as to the medial-lateral axis. The fact that there are some differences in the orientation of the border based on DTI and fMRI data in addition to the seed regions used,

indicates the need for investigation in a larger number of participants across both modalities.

Data and code availability statement

The data used in this study were obtained from the MGH-USC Human Connectome project, and are publicly available from https://ida.loni.usc.edu and http://db.humanconnectome.org.

The following, freely available code/toolboxes were used in this study: FreeSurfer (version 7.1.1, https://surfer.nmr.mgh.harvard.edu/), FMRIB Software Library's (FSL, version 5.0.9; http://fsl.fmrib.ox.ac.uk/fsl/), and Advanced Neuroimaging Toolbox (ANTs, version 2.3.4; http://stnava.github.io/ANTs/).

CRediT authorship contribution statement

Ingrid Framås Syversen: Conceptualization, Methodology, Software, Formal analysis, Investigation, Writing – original draft, Writing – review & editing, Visualization. **Menno P. Witter:** Methodology, Validation, Writing – review & editing. **Asgeir Kobro-Flatmoen:** Validation, Writing – review & editing. **Pål Erik Goa:** Conceptualization, Methodology, Resources, Writing – review & editing, Supervision, Funding acquisition. **Tobias Navarro Schröder:** Conceptualization, Methodology, Validation, Writing – review & editing, Supervision. **Christian F. Doeller:** Conceptualization, Validation, Writing – review & editing, Supervision, Funding acquisition.

Declaration of Competing Interest

The authors declare no competing interests.

Credit authorship contribution statement

Ingrid Framås Syversen: Conceptualization, Methodology, Software, Formal analysis, Investigation, Writing – original draft, Writing – review & editing, Visualization. **Menno P. Witter:** Methodology, Validation, Writing – review & editing. **Asgeir Kobro-Flatmoen:** Validation, Writing – review & editing. **Pål Erik Goa:** Conceptualization, Methodology, Resources, Writing – review & editing, Supervision, Funding acquisition. **Tobias Navarro Schröder:** Conceptualization, Methodology, Validation, Writing – review & editing, Supervision. **Christian F. Doeller:** Conceptualization, Validation, Writing – review & editing, Supervision, Funding acquisition.

Acknowledgments

Supplementary materials

Supplementary material associated with this article can be found, in the online version, at doi:10.1016/j.neuroimage.2021.118723.

References

Amunts, K., Mohlberg, H., Bludau, S., Zilles, K., 2020. Julich-Brain: a 3D probabilistic atlas of the human brain's cytoarchitecture. Science 369, 988–992. doi:10.1126/science.abb4588.

Augustinack, J., Helmer, K., Huber, K., Kakunoori, S., Zöllei, L., Fischl, B., 2010. Direct visualization of the perforant pathway in the human brain with *ex vivo* diffusion tensor imaging. Front. Hum. Neurosci. 4. doi:10.3389/fnhum.2010.00042.

Avants, B.B., Tustison, N.J., Song, G., Cook, P.A., Klein, A., Gee, J.C., 2011. A reproducible evaluation of ANTs similarity metric performance in brain image registration. Neuroimage 54, 2033–2044. doi:10.1016/j.neuroimage.2010.09.025.

Behrens, T.E., Johansen-Berg, H., Jbabdi, S., Rushworth, M.F., Woolrich, M.W., 2007. Probabilistic diffusion tractography with multiple fibre orientations: what can we gain? Neuroimage 34, 144–155. doi:10.1016/j.neuroimage.2006.09.018.

Behrens, T.E., Johansen-Berg, H., Woolrich, M.W., Smith, S.M., Wheeler-Kingshott, C.A., Boulby, P.A., Barker, G.J., Sillery, E.L., Sheehan, K., Ciccarelli, O., Thompson, A.J., Brady, J.M., Matthews, P.M., 2003a. Non-invasive mapping of connections between human thalamus and cortex using diffusion imaging. Nat. Neurosci. 6, 750–757. doi:10.1038/nn1075.

Behrens, T.E., Woolrich, M.W., Jenkinson, M., Johansen-Berg, H., Nunes, R.G., Clare, S., Matthews, P.M., Brady, J.M., Smith, S.M., 2003b. Characterization and propagation of uncertainty in diffusion-weighted MR imaging. Magn Reson Med 50, 1077–1088. doi:10.1002/mrm.10609.

Bellmund, J.L., Deuker, L., Doeller, C.F., 2019. Mapping sequence structure in the human lateral entorhinal cortex. eLife 8. doi:10.7554/eLife.45333.

Bellmund, J.L.S., Deuker, L., Navarro Schröder, T., Doeller, C.F., 2016. Grid-cell representations in mental simulation. eLife 5, e17089. doi:10.7554/eLife.17089.

Berron, D., Vogel, J.W., Insel, P.S., Pereira, J.B., Xie, L., Wisse, L.E.M., Yushkevich, P.A., Palmqvist, S., Mattsson-Carlgren, N., Stomrud, E., Smith, R., Strandberg, O., Hansson, O., 2021. Early stages of tau pathology and its associations with functional connectivity, atrophy and memory. Brain doi:10.1093/brain/awab114.

Buzsáki, G., 1996. The hippocampo-neocortical dialogue. Cereb. Cortex 6, 81–92. doi:10.1093/cercor/6.2.81.

Caballero-Bleda, M., Witter, M.P., 1993. Regional and laminar organization of projections from the presubiculum and parasubiculum to the entorhinal cortex: an anterograde tracing study in the rat. J. Comp. Neurol. 328, 115–129. doi:10.1002/cne.903280109.

Canto, C.B., Wouterlood, F.G., Witter, M.P., 2008. What does the anatomical organization of the entorhinal cortex tell us? Neural Plast. 2008, 381243. doi:10.1155/2008/381243.

Chen, X., Vieweg, P., Wolbers, T., 2019. Computing distance information from landmarks and self-motion cues - differential contributions of anterior-lateral vs. posterior-medial entorhinal cortex in humans. Neuroimage 202, 116074. doi:10.1016/j.neuroimage.2019.116074.

Deshmukh, S.S., Knierim, J.J., 2011. Representation of non-spatial and spatial information in the lateral entorhinal cortex. Front. Behav. Neurosci. 5, 69. doi:10.3389/fnbeh.2011.00069.

Doan, T.P., Lagartos-Donate, M.J., Nilssen, E.S., Ohara, S., Witter, M.P., 2019. Convergent projections from perirhinal and postrhinal cortices suggest a multisensory nature of lateral, but not medial, entorhinal cortex. Cell Rep. 29, 617–627. doi:10.1016/j.celrep.2019.09.005, .e617.

Doeller, C.F., Barry, C., Burgess, N., 2010. Evidence for grid cells in a human memory network. Nature 463, 657–661. doi:10.1038/nature08704.

Eichenbaum, H., Yonelinas, A.P., Ranganath, C., 2007. The medial temporal lobe and recognition memory. Annu. Rev. Neurosci. 30, 123–152. doi:10.1146/annurev.neuro.30.051606.094328.

Ezra, M., Faull, O.K., Jbabdi, S., Pattinson, K.T., 2015. Connectivity-based segmentation of the periaqueductal gray matter in human with brainstem optimized diffusion MRI. Hum. Brain Mapp. 36, 3459–3471. doi:10.1002/hbm.22855.

Fan, Q., Nummenmaa, A., Witzel, T., Zanzonico, R., Keil, B., Cauley, S., Polimeni, J.R., Tisdall, D., Van Dijk, K.R., Buckner, R.L., Wedeen, V.J., Rosen, B.R., Wald, L.L., 2014. Investigating the capability to resolve complex white matter structures with high *b*-value diffusion magnetic resonance imaging on the MGH-USC Connectom scanner. Brain Connect. 4, 718–726. doi:10.1089/brain.2014.0305.

Fan, Q., Witzel, T., Nummenmaa, A., Van Dijk, K.R.A., Van Horn, J.D., Drews, M.K., Somerville, L.H., Sheridan, M.A., Santillana, R.M., Snyder, J., Hedden, T., Shaw, E.E., Hollinshead, M.O., Renvall, V., Zanzonico, R., Keil, B., Cauley, S., Polimeni, J.R., Tisdall, D., Buckner, R.L., Wedeen, V.J., Wald, L.L., Toga, A.W., Rosen, B.R., 2016. MGH-USC human connectome project datasets with ultra-high *b*-value diffusion MRI. Neuroimage 124, 1108–1114. doi:10.1016/j.neuroimage.2015.08.075.

Fischl, B., Salat, D.H., Busa, E., Albert, M., Dieterich, M., Haselgrove, C., van der Kouwe, A., Killiany, R., Kennedy, D., Klaveness, S., Montillo, A., Makris, N., Rosen, B., Dale, A.M., 2002. Whole brain segmentation: automated labeling of neuroanatomical structures in the human brain. Neuron 33, 341–355. doi:10.1016/s0896-6273(02)00569-x.

Fischl, B., van der Kouwe, A., Destrieux, C., Halgren, E., Ségonne, F., Salat, D.H., Busa, E., Seidman, L.J., Goldstein, J., Kennedy, D., Caviness, V., Makris, N., Rosen, B., Dale, A.M., 2004. Automatically parcellating the human cerebral cortex. Cereb. Cortex 14, 11–22. doi:10.1093/cercor/bhg087.

Fonov, V.S., Evans, A.C., McKinstry, R.C., Almli, C.R., Collins, D.L., 2009. Unbiased nonlinear average age-appropriate brain templates from birth to adulthood. Neuroimage 47, S102. doi:10.1016/S1053-8119(09)70884-5.

Fyhn, M., Molden, S., Witter, M.P., Moser, E.I., Moser, M.B., 2004. Spatial representation in the entorhinal cortex. Science 305, 1258–1264. doi:10.1126/science.1099901.

Hafting, T., Fyhn, M., Molden, S., Moser, M.B., Moser, E.I., 2005. Microstructure of a spatial map in the entorhinal cortex. Nature 436, 801–806. doi:10.1038/nature03721.

Honda, Y., Ishizuka, N., 2004. Organization of connectivity of the rat presubiculum: I. Efferent projections to the medial entorhinal cortex. J. Comp. Neurol. 473, 463–484. doi:10.1002/cne.20093.

Hoover, W.B., Vertes, R.P., 2007. Anatomical analysis of afferent projections to the medial prefrontal cortex in the rat. Brain Struct. Funct. 212, 149–179. doi:10.1007/s00429-007-0150-4.

Howard, Lorelei R., Javadi, Amir H., Yu, Y., Mill, Ravi D., Morrison, Laura C., Knight, R., Loftus, Michelle M., Staskute, L., Spiers, Hugo J., 2014. The hippocampus and entorhinal cortex encode the path and euclidean distances to goals during navigation. Curr. Biol. 24, 1331–1340. doi:10.1016/j.cub.2014.05.001.

Huang, C.C., Rolls, E.T., Hsu, C.C.H., Feng, J., Lin, C.P., 2021. Extensive cortical connectivity of the human hippocampal memory system: beyond the "what" and "where" dual stream model. Cereb. Cortex doi:10.1093/cercor/bhab113.

Huang, H., Ding, M., 2016. Linking functional connectivity and structural connectivity quantitatively: a comparison of methods. Brain Connect. 6, 99–108. doi:10.1089/brain.2015.0382.

Høydal, Ø.A., Skytøen, E.R., Andersson, S.O., Moser, M.B., Moser, E.I., 2019. Object-vector coding in the medial entorhinal cortex. Nature 568, 400–404. doi:10.1038/s41586-019-1077-7.

Iglesias, J.E., Augustinack, J.C., Nguyen, K., Player, C.M., Player, A., Wright, M., Roy, N., Frosch, M.P., McKee, A.C., Wald, L.L., Fischl, B., Van Leemput, K., 2015. A computational atlas of the hippocampal formation using *ex vivo*, ultra-high resolution MRI: application to adaptive segmentation of *in vivo* MRI. Neuroimage 115, 117–137. doi:10.1016/j.neuroimage.2015.04.042.

Insausti, R., Amaral, D.G., 2008. Entorhinal cortex of the monkey: IV. Topographical and laminar organization of cortical afferents. J. Comp. Neurol. 509, 608–641. doi:10.1002/cne.21753.

Insausti, R., Tuñón, T., Sobreviela, T., Insausti, A.M., Gonzalo, L.M., 1995. The human entorhinal cortex: a cytoarchitectonic analysis. J. Comp. Neurol. 355, 171–198. doi:10.1002/cne.903550203.

Jenkinson, M., Beckmann, C.F., Behrens, T.E., Woolrich, M.W., Smith, S.M., 2012. FSL. Neuroimage 62, 782–790. doi:10.1016/j.neuroimage.2011.09.015.

Johansen-Berg, H., Behrens, T.E., Robson, M.D., Drobnjak, I., Rushworth, M.F., Brady, J.M., Smith, S.M., Higham, D.J., Matthews, P.M., 2004. Changes in connectivity profiles define functionally distinct regions in human medial frontal cortex. Proc. Natl. Acad. Sci. U.S.A. 101, 13335–13340. doi:10.1073/pnas.0403743101.

Jones, B.F., Witter, M.P., 2007. Cingulate cortex projections to the parahippocampal region and hippocampus in the rat. Hippocampus 17, 957–976. doi:10.1002/hipo.20330.

Kerr, K.M., Agster, K.L., Furtak, S.C., Burwell, R.D., 2007. Functional neuroanatomy of the parahippocampal region: the lateral and medial entorhinal areas. Hippocampus 17, 697–708. doi:10.1002/hipo.20315.

Khan, U.A., Liu, L., Provenzano, F.A., Berman, D.E., Profaci, C.P., Sloan, R., Mayeux, R., Duff, K.E., Small, S.A., 2014. Molecular drivers and cortical spread of lateral entorhinal cortex dysfunction in preclinical Alzheimer's disease. Nat. Neurosci. 17, 304–311. doi:10.1038/nn.3606.

Knierim, J.J., Neunuebel, J.P., Deshmukh, S.S., 2014. Functional correlates of the lateral and medial entorhinal cortex: objects, path integration and local-global reference frames. Philos. Trans. R. Soc. Lond. B Biol. Sci. 369, 20130369. doi:10.1098/rstb.2013.0369.

Kondo, H., Witter, M.P., 2014. Topographic organization of orbitofrontal projections to the parahippocampal region in rats. J. Comp. Neurol. 522, 772–793. doi:10.1002/cne.23442.

Krimer, L.S., Hyde, T.M., Herman, M.M., Saunders, R.C., 1997. The entorhinal cortex: an examination of cyto- and myeloarchitectonic organization in humans. Cereb. Cortex 7, 722–731. doi:10.1093/cercor/7.8.722.

Kulason, S., Tward, D.J., Brown, T., Sicat, C.S., Liu, C.F., Ratnanather, J.T., Younes, L., Bakker, A., Gallagher, M., Albert, M., Miller, M.I., 2019. Cortical thickness atrophy in the transentorhinal cortex in mild cognitive impairment. NeuroImage Clin. 21, 101617. doi:10.1016/j.nicl.2018.101617.

Lavenex, P., Amaral, D.G., 2000. Hippocampal-neocortical interaction: a hierarchy of associativity. Hippocampus 10, 420–430. doi:10.1002/1098-1063(2000)10:4-420::Aid-hipo8-3.0.Co;2-5.

Máté, A., Kis, D., Czigner, A., Fischer, T., Halász, L., Barzó, P., 2018. Connectivity-based segmentation of the brainstem by probabilistic tractography. Brain Res. 1690, 74–88. doi:10.1016/j.brainres.2018.03.010.

McNab, J.A., Edlow, B.L., Witzel, T., Huang, S.Y., Bhat, H., Heberlein, K., Feiweier, T., Liu, K., Keil, B., Cohen-Adad, J., Tisdall, M.D., Folkerth, R.D., Kinney, H.C., Wald, L.L., 2013. The human connectome project and beyond: initial applications of 300 mT/m gradients. Neuroimage 80, 234–245. doi:10.1016/j.neuroimage.2013.05.074.

Messé, A., Benali, H., Marrelec, G., 2015. Relating structural and functional connectivity in MRI: a simple model for a complex brain. IEEE Trans. Med. Imaging 34, 27–37. doi:10.1109/tmi.2014.2341732.

Montchal, M.E., Reagh, Z.M., Yassa, M.A., 2019. Precise temporal memories are supported by the lateral entorhinal cortex in humans. Nat. Neurosci. 22, 284–288. doi:10.1038/s41593-018-0303-1.

Mori, S., Crain, B.J., Chacko, V.P., van Zijl, P.C., 1999. Three-dimensional tracking of axonal projections in the brain by magnetic resonance imaging. Ann. Neurol. 45, 265–269 doi:10.1002/1531-8249(199902)45:2<265::aid-ana21>3.0.co;2-3.

Mori, S., Zhang, J., 2006. Principles of diffusion tensor imaging and its applications to basic neuroscience research. Neuron 51, 527–539. doi:10.1016/j.neuron.2006.08.012.

Moser, Edvard I., Moser, M.B., 2013. Grid cells and neural coding in high-end cortices. Neuron 80, 765–774. doi:10.1016/j.neuron.2013.09.043.

Maass, A., Berron, D., Libby, L.A., Ranganath, C., Düzel, E., 2015. Functional subregions of the human entorhinal cortex. eLife 4, e06426. doi:10.7554/eLife.06426.

Navarro Schröder, T., Haak, K.V., Zaragoza Jimenez, N.I., Beckmann, C.F., Doeller, C.F., 2015. Functional topography of the human entorhinal cortex. eLife 4, e06738. doi:10.7554/eLife.06738.

Nilssen, E.S., Doan, T.P., Nigro, M.J., Ohara, S., Witter, M.P., 2019. Neurons and networks in the entorhinal cortex: a reappraisal of the lateral and medial entorhinal subdivisions mediating parallel cortical pathways. Hippocampus 29, 1238–1254. doi:10.1002/hipo.23145.

Powell, H.W., Guye, M., Parker, G.J., Symms, M.R., Boulby, P., Koepp, M.J., Barker, G.J., Duncan, J.S., 2004. Noninvasive *in vivo* demonstration of the connections of the human parahippocampal gyrus. Neuroimage 22, 740–747. doi:10.1016/j.neuroimage.2004.01.011.

Ranganath, C., Ritchey, M., 2012. Two cortical systems for memory-guided behaviour. Nat. Rev. Neurosci. 13, 713–726. doi:10.1038/nrn3338.

Reagh, Z.M., Yassa, M.A., 2014. Object and spatial mnemonic interference differentially engage lateral and medial entorhinal cortex in humans. Proc. Natl. Acad. Sci. 111, E4264–E4273. doi:10.1073/pnas.1411250111.

Saleem, K.S., Kondo, H., Price, J.L., 2008. Complementary circuits connecting the orbital and medial prefrontal networks with the temporal, insular, and opercular cortex in the macaque monkey. J. Comp. Neurol. 506, 659–693. doi:10.1002/cne.21577.

Saygin, Z.M., Osher, D.E., Augustinack, J., Fischl, B., Gabrieli, J.D., 2011. Connectivity-based segmentation of human amygdala nuclei using probabilistic tractography. Neuroimage 56, 1353–1361. doi:10.1016/j.neuroimage.2011.03.006.

Schultz, H., Sommer, T., Peters, J., 2012. Direct evidence for domain-sensitive functional subregions in human entorhinal cortex. J. Neurosci. 32, 4716–4723. doi:10.1523/jneurosci.5126-11.2012.

Setsompop, K., Kimmlingen, R., Eberlein, E., Witzel, T., Cohen-Adad, J., McNab, J.A., Keil, B., Tisdall, M.D., Hoecht, P., Dietz, P., Cauley, S.F., Tountcheva, V., Matschl, V., Lenz, V.H., Heberlein, K., Potthast, A., Thein, H., Van Horn, J., Toga, A., Schmitt, F., Lehne, D., Rosen, B.R., Wedeen, V., Wald, L.L., 2013. Pushing the limits of *in vivo* diffusion MRI for the Human connectome project. Neuroimage 80, 220–233. doi:10.1016/j.neuroimage.2013.05.078.

Smith, S.M., 2002. Fast robust automated brain extraction. Hum. Brain Mapp. 17, 143–155. doi:10.1002/hbm.10062.

Sotiropoulos, S.N., Hernández-Fernández, M., Vu, A.T., Andersson, J.L., Moeller, S., Yacoub, E., Lenglet, C., Ugurbil, K., Behrens, T.E.J., Jbabdi, S., 2016. Fusion in diffusion MRI for improved fibre orientation estimation: an application to the 3T and 7T data of the Human connectome project. Neuroimage 134, 396–409. doi:10.1016/j.neuroimage.2016.04.014.

Suzuki, W.A., Eichenbaum, H., 2000. The neurophysiology of memory. Ann. N. Y. Acad. Sci. 911, 175–191. doi:10.1111/j.1749-6632.2000.tb06726.x.

Tsao, A., Moser, M.B., Moser, E.I., 2013. Traces of experience in the lateral entorhinal cortex. Curr. Biol. 23, 399–405. doi:10.1016/j.cub.2013.01.036.

Tsao, A., Sugar, J., Lu, L., Wang, C., Knierim, J.J., Moser, M.B., Moser, E.I., 2018. Integrating time from experience in the lateral entorhinal cortex. Nature 561, 57–62. doi:10.1038/s41586-018-0459-6.

Van Dijk, K.R., Hedden, T., Venkataraman, A., Evans, K.C., Lazar, S.W., Buckner, R.L., 2010. Intrinsic functional connectivity as a tool for human connectomics: theory, properties, and optimization. J. Neurophysiol. 103, 297–321. doi:10.1152/jn.00783.2009.

van Strien, N.M., Cappaert, N.L.M., Witter, M.P., 2009. The anatomy of memory: an interactive overview of the parahippocampal–hippocampal network. Nat. Rev. Neurosci. 10, 272–282. doi:10.1038/nrn2614.

Witter, M.P., Amaral, D.G., 1991. Entorhinal cortex of the monkey: V. Projections to the dentate gyrus, hippocampus, and subicular complex. J. Comp. Neurol. 307, 437–459. doi:10.1002/cne.903070308.

Witter, M.P., Amaral, D.G., 2021. The entorhinal cortex of the monkey: VI. Organization of projections from the hippocampus, subiculum, presubiculum, and parasubiculum. J. Comp. Neurol. 529, 828–852. doi:10.1002/cne.24983.

Witter, M.P., Doan, T.P., Jacobsen, B., Nilssen, E.S., Ohara, S., 2017. Architecture of the entorhinal cortex A review of entorhinal anatomy in rodents with some comparative notes. Front. Syst. Neurosci. 11. doi:10.3389/fnsys.2017.00046.

Wyss, J.M., Van Groen, T., 1992. Connections between the retrosplenial cortex and the hippocampal formation in the rat: a review. Hippocampus 2, 1–11. doi:10.1002/hipo.450020102.

Zeineh, M.M., Holdsworth, S., Skare, S., Atlas, S.W., Bammer, R., 2012. Ultra-high resolution diffusion tensor imaging of the microscopic pathways of the medial temporal lobe. Neuroimage 62, 2065–2082. doi:10.1016/j.neuroimage.2012.05.065.